Analytic Expressions for the Ultimate Intrinsic Signal-to-Noise Ratio and Ultimate Intrinsic Specific Absorption Rate in MRI

E. Kopanoglu,[1,2] V. B. Erturk,[1] and E. Atalar[1,2]*

The ultimate intrinsic signal-to-noise ratio is the highest possible signal-to-noise ratio, and the ultimate intrinsic specific absorption rate provides the lowest limit of the specific absorption rate for a given flip angle distribution. Analytic expressions for ultimate intrinsic signal-to-noise ratio and ultimate intrinsic specific absorption rate are obtained for arbitrary sample geometries. These expressions are valid when the distance between the point of interest and the sample surface is smaller than the wavelength, and the sample is homogeneous. The dependence on the sample permittivity, conductivity, temperature, size, and the static magnetic field strength is given in analytic form, which enables the easy evaluation of the change in signal-to-noise ratio and specific absorption rate when the sample is scaled in size or when any of its geometrical or electrical parameters is altered. Furthermore, it is shown that signal-to-noise ratio and specific absorption rate are independent of the permeability of the sample. As a practical case and a solution example, a uniform, circular cylindrically shaped sample is studied. **Magn Reson Med 66:846–858, 2011. © 2011 Wiley-Liss, Inc.**

Key words: ultimate intrinsic SNR; ultimate intrinsic SAR; quasi-static

INTRODUCTION

In magnetic resonance imaging (MRI), increasing signal-to-noise ratio (SNR) improves the quality of acquired images, resulting in an easier diagnosis. Therefore, numerous studies have been conducted to maximize SNR in the form of understanding the main noise sources in MRI experiments and minimizing their contributions. The main noise sources in an MRI experiment can be classified as the preamplifier, the coil, and the sample (1). Preamplifier noise is small when ultra-low-noise amplifiers are utilized (2). Coil noise is also small in most applications (3). Although it becomes dominant when low-field imaging and/or small coils are used, its effect can be minimized using superconductor or low temperature wires (4–6).

Consequently, in the majority of MRI applications, sample noise becomes the dominant factor in the determination of the SNR of images.

Because the SNR of an image depends on many factors, it may not serve as a good measure of coil performance. As an alternative, intrinsic SNR (ISNR) has been defined by removing the imaging parameter-dependent components and making it dependent only on the coil structure and the geometric and electromagnetic properties of the sample of interest. Therefore, the lowest upper bound on ISNR, which is called ultimate ISNR (UISNR) (7), provides a solid reference for coil performance evaluations.

On the other hand, minimization of the specific absorption rate (SAR) is fundamental in decreasing the adverse effects on patients, and similar to UISNR, a relative measure of the lowest possible SAR, the ultimate intrinsic SAR (UISAR) has been defined (8). Furthermore, UISNR and UISAR are related due to two reasons: first, the transmission field and receiver sensitivity of a coil are related through the reciprocity principle (9,10); second, the absorbed power in the sample that is used for SAR calculations is a function of the same loss mechanism that is responsible for the thermal noise in the UISNR calculations. This topic will be explained in more detail in Section Ultimate Intrinsic Specific Absorption Rate and Appendix A.

The semianalytic and analytic methods (which refer to methods for which computational implementation is and is not needed, respectively) in the literature for the calculation of UISNR and UISAR are limited to semi-infinite planar, spherical, and cylindrical sample geometries (7,8, 11–26). The main reason behind this limitation is the lack of appropriate basis functions that are used to express the electromagnetic field inside a sample. It is known that the choice of basis functions affects the computation time and the numerical error (8,11). The use of basis functions whose functional form resemble the exact field decreases the necessary number of modes and, hence, the computation time. However, such basis functions are hard to find when the sample shape is arbitrary. Nevertheless, plane waves and cylindrical and spherical harmonics can still be employed for arbitrary geometries. However, the required number of modes and consequently the computation time increase significantly for such basis functions. Furthermore, these methods will be more prone to error (which will be referred to in Section A Practical Implementation: Cylindrical Samples). Thus, finding an appropriate set of basis functions for an arbitrary geometry is difficult.

Throughout the years, numerous studies have been conducted in the literature about UISNR and UISAR. Ocali and

Atalar (7) concentrated on elliptical cylinders, whereas, in other work, the sample geometry was a cylinder with a circular cross section (12). A cylindrical geometry was also investigated by Vesselle and Collin (13). Ohliger et al. (14) adapted the UISNR theory to parallel imaging to investigate the effect of acceleration for an elliptical cylindrical sample. Wiesinger et al. (15,16) studied a spherical geometry when parallel MRI was used and showed that UISNR could be approached using loop coils (16). Coil performance maps, which measure the performance of actual coil arrays with respect to UISNR, were shown in (11) for the case of a cylindrical sample with a circular cross section for parallel MRI. Schnell et al. (17) investigated the performance of various practical geometries for infinite half-space and cylinder cases. UISNR and UISAR were studied by Lattanzi et al. for cylindrical and spherical samples (8,18–20). Eryaman et al. found the optimum SAR distribution for a given flip angle distribution (21). All of these studies used semianalytic methods to calculate UISNR and UISAR. In the obtained expressions, various mathematical functions such as Bessel functions or operations such as integrations or matrix multiplications exist. As the static magnetic field strength and sample-related parameters are used as arguments of these functions and operations, the effect of these parameters on UISNR and UISAR is not explicit in these studies.

On the other hand, there are analytic studies in the literature that show explicitly the dependence of UISNR and UISAR on sample-related parameters and the static magnetic field strength. In analytic studies, Hoult and Lauterbur (22) obtained the SNR limits for a spherical geometry, and Wang et al. (23) and Reykowski (24,25) found the ultimate SNR limits of circular and square loop coils when the sample was a dielectric half-space or a dielectric cylinder, respectively. An analytic expression for UISNR when the point of interest is the center of a cylinder was found by Kopanoglu et al. (26). However, all of these studies (analytic and semianalytic) were restricted to spherical, cylindrical, and semi-infinite planar samples only. As a result, there is no method in the literature that provides intuitive information (i.e., shows explicitly the dependence of UISNR and UISAR on the sample parameters and other variables) about the UISNR and UISAR for an arbitrarily shaped sample.

Motivated by this, we present analytic expressions to approximate UISNR and UISAR values for arbitrary sample geometries. To derive the analytic expressions, we define a shape and a size factor that are specific to the MRI experiment. The shape factor depends on the coil configuration, the shape of the sample, and the relative position of the point of interest (POI) in the sample. However, it is independent of sample parameters, including the size, permittivity, permeability, conductivity, temperature, nucleus of interest, and the static magnetic field strength. The shape factor can be calculated either using numerical methods, or CAD tools, or analytic methods. The expressions for UISNR and UISAR are derived by finding the maximum value of the shape factor, which is for the optimal coil configuration. Our expressions explicitly show how UISNR and UISAR depend on the main magnetic field and on the sample-related parameters mentioned above. It is also shown that UISNR and UISAR are independent of the permeability of the sample. These expressions are valid when the distance between the coil and the POI is smaller than the wavelength, which is referred to as the quasi-static limit throughout the article. As a practical case and a solution example, UISNR and UISAR expressions are presented for a uniform and electrically small sample in the shape of a circular cylinder. Using this example solution, it is shown that the error is below 1%, 10%, and 25%, when the coil-POI distance is smaller than one-tenth, one-fifth, and one-third of the wavelength, respectively.

THEORY

Quasi-Static Limit

In this article, the "quasi-static limit" means that, the distance, r_s, between the source and observation points is electrically small (i.e., with respect to the wavelength, λ) such that the phase and amplitude variations of the electromagnetic field due to wavelength and conductivity are negligible along this distance. This condition corresponds to $|kr_s| \ll 1$ (i.e., $r_s \ll 1/|k|$), where $k = \omega_0 \sqrt{\mu\epsilon}\sqrt{1 - j\tan\delta}$ is the complex wavenumber, $\tan\delta = \sigma/(\omega_0\epsilon)$ is the loss tangent, and ϵ, μ and σ are the permittivity, permeability, and conductivity of the sample, respectively. Finally, note that throughout this article, the operating frequency is ω_0, which is the Larmor frequency, and is related to the static magnetic field strength, B_0, via $\omega_0 = \gamma B_0$ where γ is the gyromagnetic ratio.

A collection of two opposite charges that lie close to each other in space is called an electric dipole, whereas a small loop coil is called a magnetic dipole (27), and they are the most basic radiating elements in electromagnetics. Hence, any current distribution can be expressed as a collection of either electric or magnetic dipoles or both. When their field expressions are used without any simplifications, an electric dipole can be replaced by a group of magnetic dipoles and vice versa (17). However, in the quasi-static limit, the expressions can be simplified by retaining only the terms that contribute the most, which then requires the utilization of both types of dipoles to form a complete set of basis functions. Note that in the quasi-static limit, the electric and magnetic fields of an electric dipole vary with $1/r_s^3$ and $1/r_s^2$, whereas it is $1/r_s^2$ and $1/r_s^3$, respectively, for the magnetic dipole. Because the magnetic field is the source signal and the electric field contributes to noise in MRI, the ratio of $|H/E|$ should be maximized for maximum SNR. At the quasi-static limit, $|H/E|$ varies with r_s for electric dipoles and with $1/r_s$ for magnetic dipoles and, therefore, approaches 0 for the former and ∞ the latter as the sample size becomes smaller. As a consequence, magnetic dipoles are the meaningful choice of radiating elements (without any need for electric dipoles). Furthermore, it was previously shown (15,23) that magnetic dipoles can be employed to approach UISNR. Hence, magnetic dipoles will be used as coil elements for UISNR and UISAR calculations in the following sections.

A special case that should be considered here is when the sample size is comparable with the wavelength but the distance between the POI and the surface is much smaller than the wavelength. In such a case, it is well known that the optimum coil structure will be a group of coils that are as close to the POI as possible. Due to two reasons, namely,

the decay of the field of magnetic dipoles with distance and the conductivity of the sample, the RF power will decay to negligible levels away from the POI into the sample. This decay distance will be in or close to the quasi-static regime. Hence, this behavior renders our formulation presented in the following sections to be valid for this special case. This argument will be supported with simulation results in the Results section.

Electromagnetic Field Expressions and Absorbed Power

The forward-polarized received magnetic field (please refer to Appendix A for the definition) and the electric field inside a homogeneous sample, generated by a group of small loop coils (magnetic dipoles) that are on the boundary of the sample, can be expressed at the quasi-static limit:

$$H_f^r(\mathbf{r}) = \sum_m \frac{a^2}{r_m^3} I_m f_m^h(\theta, \phi) e^{-jkr_m} \qquad [1]$$

$$\mathbf{E}(\mathbf{r}) = \sum_m \omega_0 \mu \frac{a^2}{r_m^2} I_m \left[\hat{\mathbf{x}} f_m^x(\theta, \phi) + \hat{\mathbf{y}} f_m^y(\theta, \phi) + \hat{\mathbf{z}} f_m^z(\theta, \phi) \right] e^{-jkr_m}$$
$$[2]$$

where the field expressions of a single loop coil are taken from (27). The hat symbol denotes a unit vector, a is the radii of the loop coils, m is the loop coil index, r_m is the distance between the mth loop's center and the POI, and I_m is the current passing through the mth coil. In Eqs. 1–2, $f_m^h(\theta, \phi)$, $f_m^x(\theta, \phi)$, $f_m^y(\theta, \phi)$ and $f_m^z(\theta, \phi)$ are functions of the spherical variables, θ and ϕ. These functions, which represent the angular weights due to the position of the POI as well as the location and orientation of the mth coil, are not given here because this is a general solution, and exact forms of such functions require well-defined geometries. It should be kept in mind that any electromagnetic field distribution should satisfy the boundary conditions. For our formulation, as the sources lay on the surface of the sample, the boundary conditions are satisfied through the sources. Although putting coils on the surface of the sample is not feasible, equivalent sources that are away from the sample can be found anytime using the Equivalence Principle (27). Because $kr_m \ll 1$ in the quasi-static limit, the exponential terms e^{-jkr_m} can be neglected.

The total absorbed power in a linear medium with conductivity σ is given in (28) as the following:

$$P = \sigma \int_V |\mathbf{E}(\mathbf{r})|^2 \, dv. \qquad [3]$$

where V is the sample volume. Note that the electric and magnetic fields are in root-mean-squared (rms) units. Equation 3 can be cast into the following form:

$$P = \sigma \omega_0^2 \mu^2 a^4 r^{-1} p \qquad [4]$$

where

$$p = \sum_{i=\{x,y,z\}} \int_V \left(\sum_m I_m f_m^i(\theta, \phi) \right)^* \left(\sum_n I_n f_n^i(\theta, \phi) \right)$$
$$\times \frac{1}{(r_m/r)^2 (r_n/r)^2} \frac{dv}{r^3} \qquad [5]$$

and the symbol * denotes the complex conjugate. Note that in Eq. 5, all coil-to-POI distance terms (r_n and r_m) are normalized with r. Here r is the size factor of the sample and can be chosen as a fundamental dimension of the sample. For example, if the sample is a cylinder, r may represent its radius; if the sample is a cube, then r may represent the length of one of its edges. As the coil-to-POI distance terms (r_n and r_m) are also dependent on the size of the sample, r_m/r and r_n/r are normalized distances. Hence, the integral is over a unit volume with the same shape as the sample, and as a result, the parameter p has units of current squared and is independent of the sample size. Let $H_f^r(\mathbf{r}_0)$ be the forward-polarized magnetic field at the POI where $\mathbf{r}_0$ is the position vector of the POI. Then the rotating magnetic field magnitude per square-root of the total absorbed power at the POI can be defined by the following equations:

$$\xi = \frac{|H_f^r(\mathbf{r}_0)|}{\sqrt{P}} \qquad [6]$$

$$= \frac{1}{\omega_0 \mu \sqrt{\sigma r^{-1}}} \frac{1}{\sqrt{p}} \sum_m I_m r^{-3} \frac{1}{(r_m/r)^3} f_m^h(\theta, \phi). \qquad [7]$$

$$= \mathcal{S} \frac{1}{\omega_0 \mu \sqrt{\sigma}} r^{-2.5} \qquad [8]$$

where

$$\mathcal{S} = \frac{1}{\sqrt{p}} \sum_m I_m \frac{1}{(r_m/r)^3} f_m^h(\theta, \phi) \qquad [9]$$

is a unitless function that depends on the POI, the shape of the sample and the coil structure. Note that $\mathcal{S}$ is independent of the size and electrical parameters of the sample, and it will be called the shape factor throughout the paper. Although choosing different fundamental dimensions for the size factor affects the normalization in Eqs. 5 and 9, and therefore scales the value of the shape factor, this scaling is canceled in Eq. 8 by the scaling of the size factor. Hence, the value of ξ, which will be used for UISNR and UISAR calculations, remains the same. For some coil structures, the shape factor may also include electric dipole terms; however, toward reaching UISNR and UISAR at the quasi-static limit, these terms should be avoided as explained in Section Quasi-Static Limit. For an arbitrary sample shape, finding the maximum value of $\mathcal{S}$ can be carried out either analytically, by CAD tools or by using optimization methods that have been previously shown (7,8). The importance of the shape factor is that it is independent of the static magnetic field strength, the imaging parameters and the parameters of the sample such as the permittivity, permeability, conductivity, size, and temperature. Hence, the dependence of UISNR and UISAR on these parameters can be shown analytically, as will be done in the following sections. The rotating magnetic field is the signal that is used to reconstruct the images, and the total absorbed power is related to both the noise in acquired images and the heating in the sample; hence, ξ can be converted to UISNR and UISAR as will be shown in the succeeding sections.

Ultimate Intrinsic Signal-to-Noise Ratio

The SNR of an image is defined point-by-point in (3,7) as the following:

$$\text{SNR} = \Psi \Upsilon \qquad [10]$$

where

$$\Upsilon = \frac{\mathcal{V}\sqrt{N_x N_y NEX}}{\sqrt{F2BW}} w\left(T_1, T_2, T_2^*, \alpha\right) \qquad [11]$$

and

$$\Psi = \frac{\sqrt{2}\omega_0 \mu M_0}{\sqrt{4k_B TP}} \left| H_f^r \right|. \qquad [12]$$

In Eq. 11, Υ contains the imaging parameters, where F is the overall system noise figure (in terms of power), $\mathcal{V}$ is the voxel volume in cubic meters, NEX is the number of image repetitions, N_x is the number of readout points, N_y is the number of phase encoding steps, BW is the baseband receiver bandwidth and the weight function $w(T_1, T_2, T_2^*, \alpha)$ contains the effects of the flip angle α and the relaxation time constants T_1, T_2, T_2^*. In Eq. 12, Ψ is the ISNR of the coil at hand (3,7), where M_0 is the magnetization density per voxel after a 90° pulse, k_B is the Boltzmann constant and T is the sample temperature. Note that ISNR is defined point-by-point, and the ISNR of a POI at $\mathbf{r}_0$ is independent of the imaging parameters. The static magnetic field B_0 is assumed to be along the $\hat{\mathbf{z}}$-axis without loss of generality. Finally, H_f^r and P are the forward-polarized received magnetic field and the total noise power, respectively, where both are in root-mean-squared (rms) units. It should be kept in mind that for SNR calculations, the magnitude of the received forward-polarized magnetic field, defined in Electric Field Expressions inside the Sample section in Appendix B, is used. Using Eqs. 6 and 8 in Eq. 12 yields the following:

$$\text{ISNR} = \frac{\sqrt{2}M_0}{\sqrt{4k_B T\sigma}} \mathcal{S} r^{-2.5}. \qquad [13]$$

Employing the definition of M_0 as given in reference (22) to show explicitly the dependence on the static magnetic field yields Eq. 14:

$$\text{ISNR} = \frac{N\gamma^2 \hbar^2 I_z(I_z + 1)}{\sqrt{18k_B^3}} \mathcal{S} B_0 T^{-1.5} \sigma^{-0.5} r^{-2.5}. \qquad [14]$$

where N is the number of nuclear spins per unit volume, $\hbar$ is the reduced Planck constant, and I_z is the quantum spin number for the nucleus of interest. Note that although the terms of the fraction are nucleus-dependent (ex: H^+, Na^+, etc.), they are independent of the sample and the coil. Furthermore, $\mathcal{S}$ is the only term in Eq. 14 that depends on the coil geometry, the POI and the shape of the sample with the dependence on the coil geometry being due to the summations in Eqs. 1 and 2 over the coil structure. Finding the optimum coil structure that achieves UISNR corresponds to finding the maximum value of $\mathcal{S}$. Hence, an analytic expression for the UISNR can be obtained from Eq. 14 as the following:

$$\text{UISNR} = cN\gamma^2 I_z(I_z + 1)\mathcal{S}_{\max} B_0 T^{-1.5} \sigma^{-0.5} r^{-2.5}. \qquad [15]$$

where $c = 5.11 \times 10^{-35}$ is a constant with units $J^{0.5}K^{1.5}s^2$. When searching for the optimum coil structure, the optimization can be made either for a specific magnetic field value at a certain POI or for a field distribution in a certain region. Note that the shape factor is the only term in Eqs. 14 and 15, and these two cases will most probably yield different coil structures and therefore different $\mathcal{S}_{\max}$ values. However, the other terms in Eqs. 14 and 15 will be unaffected. Hence, Eq. 15 is valid for both optimization cases. Equation 15 provides intuitive information about how the UISNR and therefore the SNR depend on the size, permittivity, conductivity and temperature of the sample, and the static magnetic field strength. Furthermore, the dependence on the gyromagnetic ratio of the imaged nucleus and the available spin density (N) are explicitly given, and it is shown that SNR and UISNR are independent of the permeability of the sample.

Assuming that the number of voxels is unchanged, it can be easily shown that the dependence of the imaging parameters on the size of the sample is $\Upsilon \propto r^3$, as the voxel volume is the only size-dependent term in Υ. Hence, $\text{SNR} = \Upsilon\Psi \propto r^{0.5}\sqrt{NEX}$, and to obtain the same SNR level from two identical samples that only differ in size, the required total imaging time is given by $T_{\text{total}} \propto 1/r$.

When the size of the imaged sample becomes smaller, a very small coil is sufficient to image the sample, in which case, the total absorbed power will be limited to very low levels. As a result, the UISNR approaches infinity, which can be seen from Eq. 15 by taking the size term (i.e., r) to zero. However, a single voxel would simultaneously approach zero more rapidly (i.e., $\mathcal{V} \propto r^3$), making the SNR limit finite.

Ultimate Intrinsic Specific Absorption Rate

SAR is defined as the absorbed power by the sample per certain mass of sample. Regulatory limits are defined for 1-g, 10-g and whole-body-averaged and organ-averaged absorbed power for the head, torso, and extremities (29,30). As mentioned in the Introduction section, the absorbed power that is used for SAR calculations is the same power that creates noise during signal reception. Hence, a similar analysis can be conducted for SAR. However, there are two fundamental differences, which do not prevent a relation between SAR and SNR but should be taken into account. First, the transmitted pulse may have a time dependent envelope. Furthermore, the received forward-polarized magnetic field is used for SNR calculations, whereas the transmitted forward-polarized magnetic field should be used for SAR. However, it is well known that a coil's forward transmission field is equal to its forward reception field when the direction of the static magnetic field is flipped from the positive to the negative z-direction. Hence, the mirrored version of a transmission coil with respect to the z-axis is a receiver coil with the same shape factor. As a result, the forward transmission magnetic field can be replaced by the forward reception magnetic field without any inconvenience. Neglecting the field transients, the transmitted RF pulse (in the rotating frame, denoted by $_{\text{rot}}$) and the electric field can be expressed as the following equations:

$$_{\text{rot}}\overline{H}_{\text{f}}^{\text{t}}(\mathbf{r}, t) = \left[H_{\text{f}}^{\text{t}}(\mathbf{r})\right]^{*} g(t) \qquad [16]$$

$$\overline{\mathbf{E}}(\mathbf{r}, t) = \mathbf{E}(\mathbf{r})g(t) \qquad [17]$$

where $H_{\text{f}}^{\text{t}}(\mathbf{r})$ and $g(t)$ are the phasor domain representations of the magnetic field and the time-dependent envelope of the transmitted RF signal, respectively (the derivations are given in Appendix A). Note that the envelope function is assumed to generate a small bandwidth when compared to the Larmor frequency. The magnetic field $_{\text{rot}}\overline{H}_{\text{f}}^{\text{t}}(\mathbf{r}, t)$ leads to a flip angle distribution through the relation:

$$\alpha(\mathbf{r}, t) = \gamma\mu|H_{\text{f}}^{\text{t}}(\mathbf{r})|\overline{g} \qquad [18]$$

where $\overline{g} = \int_0^{T_R} g(t)\, dt$ is the time integral of the RF envelope $g(t)$ (please refer to Appendix A for details). The time-averaged power is given by the following equations:

$$P^{\text{av}} = \frac{1}{T_R}\int_0^{T_R}\iiint_V \sigma|\overline{\mathbf{E}}(\mathbf{r}, t)|^2\, dv\, dt \qquad [19]$$

$$= \frac{\overline{g^2}}{T_R}P \qquad [20]$$

where P is the time-independent power defined in Eq. 3, and $\overline{g^2} = \int_0^{T_R}|g(t)|^2\, dt$ is the time integral of the square of the RF envelope. Using the definitions given in Eqs. 6 and 16–20, the SAR can be expressed as the following equations:

$$\text{SAR} = \frac{P^{\text{av}}}{m_{\text{sample}}} \qquad [21]$$

$$= \frac{\overline{g^2}}{\xi^2 m_{\text{sample}} T_R}\left(\frac{\alpha}{\gamma\mu\overline{g}}\right)^2 \qquad [22]$$

The SAR can be separated into two parts, one that contains the imaging parameters and one that is independent of the imaging parameters, the latter being the Intrinsic SAR:

$$\text{SAR} = \text{ISAR}\Phi \qquad [23]$$

where

$$\Phi = \frac{\overline{g^2}\alpha^2}{\overline{g}^2 T_R} \qquad [24]$$

and

$$\text{ISAR} = \frac{1}{\xi^2\gamma^2\mu^2 m_{\text{sample}}}. \qquad [25]$$

Note that, because the quasi-static assumption has not yet been used, this ISAR definition is valid for any case. The physical interpretation of the ISAR definition is described as follows. The envelope of the transmitted signal and the flip angle are imaging parameters that affect the SAR. ISAR, on the other hand, is the total absorbed power per total sample mass for unit flip angle at a specific position $\mathbf{r}_0$ when the integral of the RF envelope and its square are equal to one. Hence, it is independent of the imaging parameters α, $\overline{g}$, and $\overline{g^2}$. Note that, ISAR is dependent on the position $\mathbf{r}_0$ because unit flip angle is assumed at $\mathbf{r}_0$. Because the location of the unit flip-angle is known, SAR and ultimate-SAR can be calculated from ISAR and UISAR, respectively.

Although, choosing an alternative unit flip-angle position scales the ISAR and UISAR; values of SAR and ultimate-SAR do not change. Similar to the ISNR, ISAR depends only on the static magnetic field strength, the coil and the sample. Therefore, it can be used for comparing coil performances.

Although the concept of ultimate-ISAR was previously studied (8), a proportional expression was given for UISAR instead of an exact formulation. Hence, this is the first time ISAR is defined.

At the quasi-static limit, by using Eq. 8, ISAR can be expressed:

$$\text{ISAR} = \frac{\sigma B_0^2 r^5}{m_{\text{sample}}\mathcal{S}^2} \qquad [26]$$

The only parameter in Eq. 26 that depends on the POI location, the shape of the sample and the coil structure is the shape factor. Hence, finding the UISAR corresponds to maximizing the shape factor, which leads to the expression:

$$\text{UISAR} = \frac{\sigma B_0^2 r^5}{m_{\text{sample}}\mathcal{S}_{\text{max}}^2}. \qquad [27]$$

Maximization of the shape factor is an optimization process, similar to obtaining UISNR from ISNR. Hence, some constraints should be set. This can be accomplished by aiming at a certain flip angle at a specific position or for a flip angle distribution among many points inside the sample. Methods for minimizing the SAR for a flip angle distribution or magnetic field distribution among many points have been shown previously (8,21). Note that the constraints should be normalized with the flip angle value used for ISAR definition, $\gamma\mu|H_{\text{f}}^{\text{t}}(\mathbf{r}_0)|$, to be consistent.

An important point is that as long as the specified field and SAR distributions are consistent with each other, the $\mathcal{S}_{\text{max}}$ values of UISNR and UISAR will be the same. Equation 27 provides intuitive information about the dependence of UISAR on the static magnetic field strength and the sample parameters including permittivity, conductivity, and size. Furthermore, it is shown that UISAR and therefore SAR are independent of the permeability of the sample.

PRACTICAL IMPLEMENTATION: CYLINDRICAL SAMPLES

In various MRI applications, such as small animal, human extremity and phantom imaging, the sample that will be imaged can be modeled by a circular cylinder (Fig. 1). Therefore, a uniform, electrically small and conductive cylindrical sample is studied as a practical case. To arrive at the UISNR and UISAR equations of the cylindrical sample, two different cases are considered: when the POI is on the axis of the cylinder and when the POI is very close to the surface. Note that single point optimizations are made for both cases. For the POI at the center, an analytic solution is obtained similar to (26). When the POI is very close to the surface, the problem is equivalent to a semi-infinite planar sample case and is replaced with the latter to find UISNR and UISAR equations for the semi-infinite planar case. Then the two cases are combined using asymptotic methods into two equations for UISNR and UISAR of the
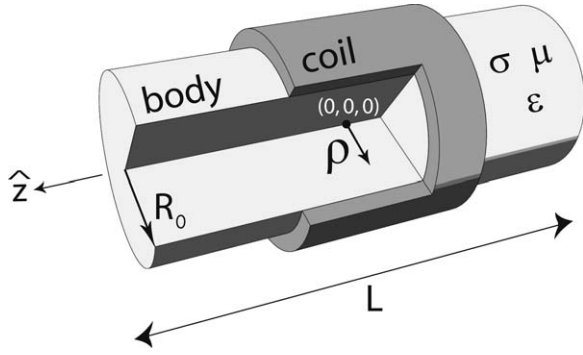
FIG. 1. Geometrical structure of the studied practical sample. R_0, L, σ, ϵ, and μ are the radius, length, conductivity, permittivity, and permeability of the sample, respectively. ρ is the radial distance from the axis of the cylinder to the POI. The region titled "coil" shows a possible location of the RF coil for better visualization of the structure, not the exact shape or position. d is defined as $d = 1 - \rho/R_0$. $d = 1$ corresponds to the axis of the sample, whereas $d = 0$ and $d = 0.5$ correspond to the surface and the half-way point between the surface and the axis of the cylinder, respectively.

cylindrical sample. For all of these cases, the resulting UISNR and UISAR expressions are in the same form as Eqs. 15 and 27.

Analytic expressions for UISNR and UISAR in a cylindrical sample when the POI is on the axis are found as follows: For a cylindrical sample aligned with the z-axis, the electric and magnetic field components along the z-axis are expressed using the cylindrical wave expansion as given in Ref. (31) and in Eqs. B.1 and B.2. Then the transverse components of the electric and magnetic fields are derived from the z components in Eq. B.3 with the aid of Maxwell's Equations (32). The received forward-polarized magnetic field is defined in Eq. B.5, and the total absorbed power is given in Eq. B.9. The minimum noise power for a preset signal strength is obtained using the Lagrange Multipliers Method (33) in Power Definition section in Appendix B (Eq. B.22). By substituting Eq. B.23 into Eq. 13, an analytic UISNR expression can be obtained for the cylindrical sample when the POI is on the axis of the cylinder. Similarly, by using Eqs. 25 and B.23 together, an analytic UISAR expression can be achieved. The shape and size factors, (i.e., $\mathcal{S}$ and r) are obtained as $\mathcal{S} = 1.035$ and $r = R_0$, where R_0 is the radius of the cylinder. In (24), Reykowski found a similar expression with $\mathcal{S} = 0.9545$ and $r = R_0$.

When the POI approaches the surface, an extremely confined field distribution created by a minute coil close to the POI is sufficient to create a signal at the POI. In that case, the effective sample seen by the coil will be a semi-infinite plane. By employing the semianalytic method given in Ref. (12), the size factor r is found to be equal to the distance between the POI and the surface, and the shape factor $\mathcal{S}$ is obtained as 0.466 for a semi-infinite planar sample. However, as mentioned in the introduction, the choice of basis functions affects the numerical error, and therefore the results, significantly. Because we performed a cylindrical wave expansion for a planar structure, the required number of modes is very high, and the shape factor has a numerical error $\sim$10%. In Ref. (23), this sample shape was

also studied and the analytical result presented (23) corresponds to a shape factor value of $\mathcal{S} = 0.423$. For the rest of our derivations, this shape factor will be used.

By employing asymptotic methods, the results for the semi-infinite planar and cylindrical samples can be combined into two equations given by the following:

$$\text{UISNR} = cN\gamma^2 I_z(I_z + 1)\mathcal{S}_{\max}^{\text{cyl}} B_0 T^{-1.5}\sigma^{-0.5}R_0^{-2.5} \qquad [28]$$

$$\text{UISAR} = \frac{\sigma B_0^2 R_0^5}{m_{\text{sample}}\left(\mathcal{S}_{\max}^{\text{cyl}}\right)^2}. \qquad [29]$$

where $\mathcal{S}_{\max}^{\text{cyl}} = 0.953\sqrt{1 + \left(0.723/d\right)^5}$. Note that the above equations are in the same form as Eqs. 15 and 27. $d = 1 - r_0/R_0$ is defined as the normalized distance between the POI and the surface of the sample (which is normalized with respect to the radius of the sample), and r_0 is the radial distance between the POI and the axis of the cylinder. Note that d is a parameter between 0 and 1, and it is independent of the size of the sample.

RESULTS

The analytic UISNR expression is compared with the semi-analytic method presented by Celik et al. (12). The percent error in the analytic expression is defined as the following:

$$\text{error}\% = 100\frac{\text{UISNR}_a - \text{UISNR}_{\text{s.a.}}}{\text{UISNR}_{\text{s.a.}}} \qquad [30]$$

where $\text{UISNR}_{\text{s.a.}}$ denotes Celik's semianalytic method solutions, and UISNR_a denotes the analytic expression given in Eq. 28. For arriving at the analytic expressions, it was assumed in Section Quasi-Static Limit that the distance between the surface and the POI is smaller than $1/|k|$. To observe the effect of this assumption on the error, the error curves in Figures 3 and 4 are plotted with respect to the normalized distance between the POI and the surface with respect to the wavelength. The wavelength and the wavenumber are related by the following equation:

$$\lambda = \frac{2\pi}{\Re\{k\}} = \frac{1}{\omega_0\sqrt{\mu\epsilon}\Re\{\sqrt{1 - j\tan\delta}\}}. \qquad [31]$$

Figure 2 shows the behavior of UISNR when the location of the POI is varied radially. Note that the vertical axis is in logarithmic scale for better understanding, and the UISNR values are normalized with respect to the value on the axis of the sample. The first important point is that the triangles, which show the data points obtained with Celik's method (12) stop at $d = 0.15$. This is because the semianalytic method is vulnerable to numerical error when the POI approaches the surface. Note that because this method is used as the reference with which the error rates are calculated, the range of d values for this and the succeeding plots are limited. Similarly, Reykowski did not calculate UISNR for $d < 0.15$ due to numerical error either (25). Instead, an analytic expression was obtained using asymptotic methods (25) that is employed here. Although the semianalytic methods fail, Reykowski's and our analytic expressions yield robust calculations for any POI location. The advantage of our analytic expression over Reykowski's method is that the dependence of UISNR on the geometrical and
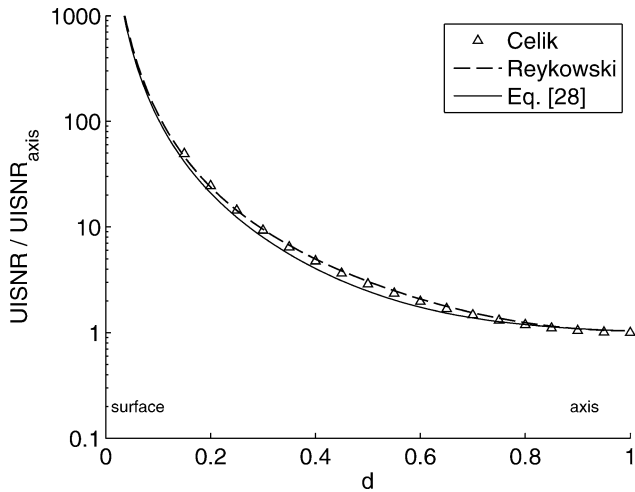
FIG. 2. UISNR values normalized with respect to the UISNR on the axis of the cylinder. The horizontal axis shows the distance between the POI and the surface normalized with respect to the radius of the cylinder, i.e., $d = 1 - \rho/R_0$. The distributions are valid for any sample parameter and field strength, as long as the distance between the POI and the surface is smaller than the wavelength, i.e., $dR_0 \ll \lambda$.

FIG. 3. The error in the analytic UISNR expression calculated by Eq. 30. The horizontal axis is the distance between the POI and the surface in terms of the wavelength (i.e., a value of 0.1 means the distance is one-tenth of the wavelength); hence, the curves represent the error behavior regardless of the field strength. The curves are for various loss tangent values. $\tan(\delta) = 0.1$ and $\tan(\delta) = 100$ curves are the approximate limits even though they do not correspond to any tissue parameters at MRI frequencies. Although $\tan(\delta) = 1.4$ and $\tan(\delta) = 2.1$ curves can represent an infinite number of permittivity, conductivity, and frequency combinations, two examples are $\sigma = 0.4\,S/m$ and $\sigma = 0.6\,S/m$, respectively, for a relative permittivity of 80 and $B_0 = 1.5\,T$.

electrical properties of the sample are given explicitly for any POI location, whereas in Reykowski's method (24,25), the dependence on sample properties is given only when the POI is at the center. Although our expression has some error when the POI is at the middle region of the sample, the error drops to negligible levels toward the axis and the surface of the sample. The maximum error was calculated to be less than 10% in our formulation.

Another important point for Fig. 2 is that the UISNR increases steeply toward the surface of the sample, approaching infinity at the surface. This is expected because when the POI is very close to the surface, a minute coil is sufficient to image the POI. With such a coil, the absorbed power is confined to an extremely small region around the POI, increasing the SNR significantly.

Figure 3 shows the error in the analytic expression given in Eq. 28 for various loss tangent values. It should be noted that loss tangent can be converted to conductivity using the formulation given in Section Quasi-Static Limit. Although they do not correspond to any tissues at MRI frequencies, $\tan(\delta) = 0.1$ and $\tan(\delta) = 100$ values are employed to illustrate the limits of the error curves. Increasing or decreasing the loss tangent beyond these values does not alter the curves significantly, and leads to numerical error in the semianalytic method given in Ref. (12). The error curves are independent of the main magnet strength and the electrical parameters of the sample, but they depend on the combination of these parameters. Therefore, as long as the loss tangent is the same, the error behaviour is the same. Hence, any curve can correspond to an infinite number of permittivity, conductivity and frequency combinations. One of these combinations for the $\tan(\delta) = 1.4$ curve is a static magnetic field strength of 1.5 T, a conductivity of 0.4 S/m and a relative permittivity of 80, which are average human body parameters at 64 MHz (34,35). For these parameters and an error margin of 20%, the obtained UISNR expression is valid as long as $dR_0 < \lambda/4$, which corresponds to a POI depth of ∼15 cm. For this plot, the POI is assumed

to be on the axis of the cylinder; however, the effect of the location of the POI is insignificant, as will be discussed in the succeeding paragraph.

For various sample sizes and POI locations, the error in the analytic UISNR expression is shown in Fig. 4, where the
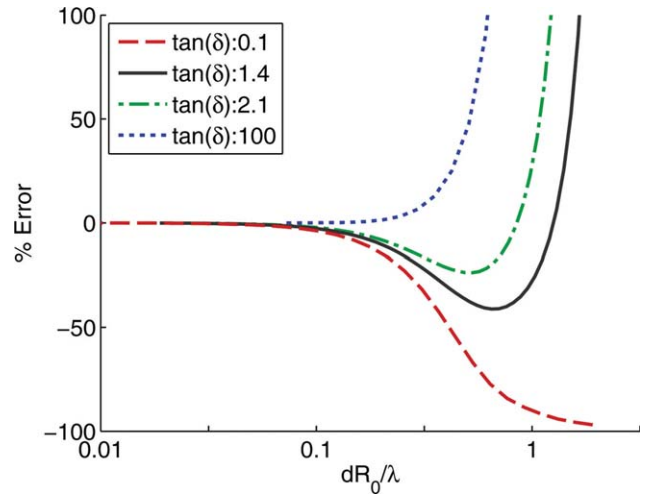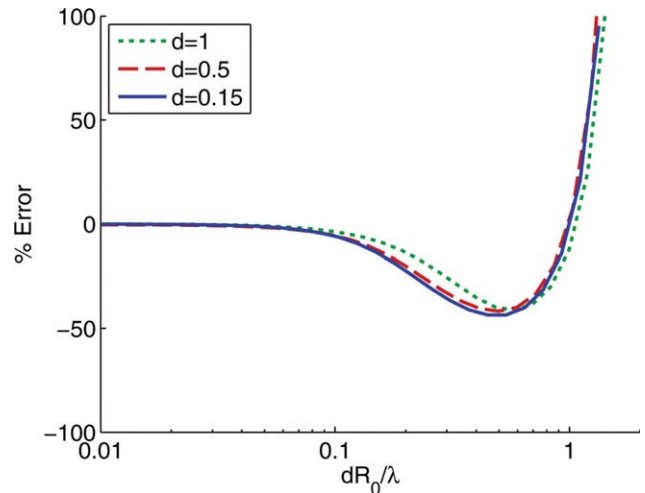

FIG. 4. The error in the analytic UISNR expression calculated by Eq. 30. The horizontal axis is the distance between the POI and the surface in terms of the wavelength (i.e., a value of 0.1 means the distance is one-tenth of the wavelength); hence, the curves represent the error behavior regardless of the field strength. The curves illustrate the behavior of the error when the POI location is altered inside the sample.

Table 1
Parameters for Some Tissues in the Human Body for 1.5T and 3T Static Magnetic Field Strengths (35)

ϵ_r (F/m)	σ (S/m)	B_0 (T)	λ (cm)	1% Error distance [cm]	10% Error distance [cm]	25% Error distance [cm]
80	0.4	1.5	40.4	2.7	8.9	15.5
60	0.5	3.0	23.9	1.6	5.0	8.5
110	0.5	1.5	34.9	2.3	7.7	13.0
70	0.7	3.0	21.6	1.5	4.7	8.1
80	0.6	1.5	37.5	2.7	9.2	38.0
60	0.8	3.0	22.2	1.6	5.2	10.5

The first two rows are for liver tissue, the third and fourth rows are for brain tissue, and the last two rows are for muscle tissue. The columns are for relative permittivity, conductivity, static magnetic field strength, wavelength, and the distances at which the error of Eq. 28 is 1%, 10%, and 25%, respectively. When calculating the error, a cylindrical sample composed of only one type of tissue is assumed.

horizontal axis is the ratio of the distance between the POI and the surface to the wavelength (i.e., electrical length). It can be seen that the error is only slightly affected when the POI location varies. Evaluating this slight change with the behavior of the error given in Fig. 3, it can be concluded that the effect of the loss tangent is much higher than the POI location, and the electrical length rather than the metric distance between the POI and the surface is a determining factor. Another important point is that if the POI is at the center, i.e., $d = 1$, a sample with radius $R_0 = \lambda/2$ has 50% error when the analytic expression is used. For the same sample, when $d = 0.15$ however, $dR_0/\lambda = 0.075$, and the error is negligible. This supports the argument that the obtained expressions are valid for samples that are comparable with the wavelength if the distance between the POI and the surface is much smaller than the wavelength.

In Table 1, the error in Eq. 28 is given for human brain, muscle and liver tissue parameters (35). Note that a cylindrical sample that is composed of only one type of tissue is assumed for the calculations. It is known from Figs. 3 and 4 that when the distance between the surface and the POI is smaller than $\lambda/10$, the error is negligible. However, for SNR calculations in MRI, larger error margins such as 10% or 25% can be employed. When the distance between the surface and the POI is close to $\lambda/5$, the error becomes 10%. When the error margin is 25%, the expressions can be used at distances up to slightly above $\lambda/3$, as shown in Table 1. As an example, when a cylindrical sample with liver parameters is imaged, UISNR of a point at a depth of 15 cm can be calculated with less than 25% error. When a similar sample with muscle properties is imaged, the expressions yield less than 25% error even at a distance of one wavelength. However, it should be kept in mind that these are example calculations. In real-life, the human body is neither cylindrical nor homogeneous, and the tissue parameters may differ from person to person; hence, these error rates may be different.

DISCUSSION AND CONCLUSIONS

In this study, analytic expressions for the UISNR and UISAR were derived. The expressions are valid as long as

the distance between the surface and the POI is smaller than the wavelength, which is referred to as the quasi-static limit. The expressions are independent of the shape of the sample that is to be imaged.

In the course of arriving at the analytic expressions, size and shape factors of a sample and coil geometry are defined. The shape factor depends on the geometrical shape of the sample and the coil structure. Hence, it is specific to the coil and sample combination. Finding the maximum value of the shape factor for all theoretically possible coil structures yields the UISNR and UISAR from the ISNR and ISAR of the sample of interest. The size factor, which is independent from the coil geometry and the sample's shape, explicitly shows the scaling of ISNR and ISAR (hence UISNR and UISAR) with any variations in the size of the sample. The shape factor is defined for the first time to the best of our knowledge. Although the dependence on the size factor was previously shown for specific geometries, it is defined for an arbitrarily shaped sample for the first time.

The derived expressions explicitly show the dependence of UISNR and UISAR on the static magnetic field strength and sample properties including the size, permittivity, conductivity, and temperature. Furthermore, it is shown that UISNR and UISAR are independent of the permeability of the sample.

Using the relations between SNR and ISNR and those between SAR and ISAR that are given in the article, the dependence of SNR and ultimate-SNR and that of SAR and ultimate-SAR on the shape and size factors and any of the other affecting parameters can be obtained easily.

The strongest aspect of the expressions given in this article comes into picture when there is a known value for SNR, SAR, UISNR, or UISAR that is obtained by experiment or by simulation. Then, these parameters can easily be calculated for a similar sample shape when any affecting parameter is altered.

Previous studies of UISNR and UISAR in the literature use optimization methods to find the UISNR and/or UISAR for either certain field/SAR distributions in the sample or certain field/SAR values at specific points. The given expressions in this article are valid for both cases. Furthermore, UISNR and UISAR were defined in the literature to form coil performance maps to evaluate coil performances and determine room for improvement. The proposed expressions can be employed for this purpose as well.

For specific geometries of interest, the dependence of UISNR on the size of the sample, i.e., $r^{-2.5}$, was shown. Hoult and Lauterbur (22) show the same dependence for a spherical sample for low frequencies, in which the size factor is the radius of the sphere. For a semi-infinite planar sample at the quasi-static limit, Wang et al. (23) show that UISNR has the same dependence in which the size factor is the distance of the POI to the surface of the sample. For a cylindrical sample, Macovski (36) has shown that the noise generated is proportional to $r_0^2 \sqrt{l}$, where r_0 is the radius, and l is the length of the cylinder. This corresponds to the ISNR part of the SNR formulation scaling with -2.5th power of the size of the cylinder. Furthermore, the ultimate SNR was shown to vary with the -2.5th power of the radius of a cylindrical sample when the POI is at the center (24,26).

These five studies show the same dependence on the size of the sample with our formulation but for specific geometries of interest.

The main limitation of the expressions given in this article is that the samples are assumed to be homogeneous during the derivations. Hence, it should be kept in mind that in real-life scenarios, samples are generally not homogeneous. Furthermore, if the distance between the POI and the surface is not in the quasi-static limit, the method introduces some error.

ACKNOWLEDGMENTS

APPENDIX A: ROTATING MAGNETIC FIELD DEFINITION

Phasor Domain

Assuming that the static magnetic field is along the $\hat{\mathbf{z}}$-axis, a general expression for the transverse magnetic field is $\overline{\mathbf{H}}(t) = \hat{\mathbf{x}}\sqrt{2}|H_x|\cos(\omega_0 t - \psi_x) + \hat{\mathbf{y}}\sqrt{2}|H_y|\cos(\omega_0 t - \psi_y)$ where $H_x = |H_x|e^{-i\psi_x}$ and $H_y = |H_y|e^{-i\psi_y}$ are the root mean square (rms) phasors of the magnetic field components along the $\hat{\mathbf{x}}$ and $\hat{\mathbf{y}}$ axes, respectively, with $|H_x|$ and $|H_y|$ being the magnitudes and ψ_x and ψ_y being the phases of the x and y components. With respect to the $\hat{\mathbf{z}}$-axis, this magnetic field can be separated into its left-hand and right-hand rotating components. During RF transmission, the right-hand-polarized component does not affect the spins, and only the left-hand component is of interest, which can be written as the following:

$$\overline{\mathbf{H}}_{\mathrm{f}}^{\mathrm{t}}(t) = |H_x|\frac{\hat{\mathbf{x}}\cos(\omega_0 t - \psi_x) - \hat{\mathbf{y}}\sin(\omega_0 t - \psi_x)}{\sqrt{2}}$$
$$+ |H_y|\frac{\hat{\mathbf{y}}\cos(\omega_0 t - \psi_y) + \hat{\mathbf{x}}\sin(\omega_0 t - \psi_y)}{\sqrt{2}} \quad [\mathrm{A.1}]$$

where the subscript $_f$ and the superscript ^{t} denote forward and transmission, respectively, meaning that this field excites the spins when used in transmission mode (37). In the phasor domain, the vector for the rms forward-polarized magnetic field can be written as $\mathbf{H}_{\mathrm{f}}^{\mathrm{t}} = \hat{\mathbf{a}}_{\mathrm{f}}^{\mathrm{t}} H_{\mathrm{f}}^{\mathrm{t}}$ where $\hat{\mathbf{a}}_{\mathrm{f}}^{\mathrm{t}} = (\hat{\mathbf{x}} + j\hat{\mathbf{y}})/\sqrt{2}$ is the forward-polarized unit vector (38), and the peak scalar forward-polarized transmission field $H_{\mathrm{f}}^{\mathrm{t}}$ is given by $H_{\mathrm{f}}^{\mathrm{t}} = H_x - jH_y$. The rms field is given by the following:

$$H_{\mathrm{f}}^{\mathrm{t}} = \frac{H_x - jH_y}{\sqrt{2}} = \frac{H_\rho - jH_\phi}{\sqrt{2}}e^{-j\phi} \quad [\mathrm{A.2}]$$

In Eq. A.2, H_ρ and H_ϕ are the magnetic field components along $\hat{\rho}$ and $\hat{\phi}$ axes of the cylindrical coordinate system, which are related to the cartesian coordinate counterparts by $H_\rho = H_x\cos(\phi) + H_y\sin(\phi)$ and $H_\phi = -H_x\sin(\phi) + H_y\cos(\phi)$. Similarly, the right-hand-polarized magnetic

field during transmission is denoted by H_{r}^{t} where the subscript $_{\mathrm{r}}$ denotes reverse-polarization. The reverse-polarized rms magnetic field and the associated unit vector are given by the following equation:

$$H_{\mathrm{r}}^{\mathrm{t}} = \frac{H_x + jH_y}{\sqrt{2}} = \frac{H_\rho + jH_\phi}{\sqrt{2}}e^{+j\phi}.$$

and $\hat{\mathbf{a}}_{\mathrm{r}}^{\mathrm{t}} = (\hat{\mathbf{x}} - j\hat{\mathbf{y}})/\sqrt{2}$. However, in signal reception, the forward-polarized unit vector is given by $\hat{\mathbf{a}}_{\mathrm{f}}^{\mathrm{r}} = [\hat{\mathbf{x}}\cos(\omega_0 t) + \hat{\mathbf{y}}\sin(\omega_0 t)]/\sqrt{2}$ for correct signal demodulation. Hence, in the phasor domain, the forward- and reverse-polarized unit vectors for reception are given by $\hat{\mathbf{a}}_{\mathrm{f}}^{\mathrm{r}} = (\hat{\mathbf{x}} - j\hat{\mathbf{y}})/\sqrt{2}$ and $\hat{\mathbf{a}}_{\mathrm{r}}^{\mathrm{r}} = (\hat{\mathbf{x}} + j\hat{\mathbf{y}})/\sqrt{2}$. Hence, the corresponding field expressions become the following:

$$H_{\mathrm{f}}^{\mathrm{r}} = \frac{H_x + jH_y}{\sqrt{2}} = \frac{H_\rho + jH_\phi}{\sqrt{2}}e^{+j\phi}$$
$$H_{\mathrm{r}}^{\mathrm{r}} = \frac{H_x - jH_y}{\sqrt{2}} = \frac{H_\rho - jH_\phi}{\sqrt{2}}e^{-j\phi}. \quad [\mathrm{A.3}]$$

Rotating Frame

For SNR calculations, a time-independent analysis can be conducted, whereas for SAR calculations, the envelope of the transmitted signal should also be considered. Letting $g(t)$ represent the envelope of the transmitted RF signal, the transmitted forward-polarized magnetic field can be expressed as the following:

$$\overline{\mathbf{H}}_{\mathrm{f}}^{\mathrm{t}}(t) = |H_x|g(t)\frac{\hat{\mathbf{x}}\cos(\omega_0 t - \psi_x) - \hat{\mathbf{y}}\sin(\omega_0 t - \psi_x)}{\sqrt{2}}$$
$$+ |H_y|g(t)\frac{\hat{\mathbf{y}}\cos(\omega_0 t - \psi_y) + \hat{\mathbf{x}}\sin(\omega_0 t - \psi_y)}{\sqrt{2}} \quad [\mathrm{A.4}]$$

It is common practice to call the x-axis the real axis, and the y-axis the imaginary axis, as suggested by the Argand diagram. Then by letting $t = 0$ to transform the lab frame to the rotating frame, the magnetic field in the rotating frame is the following:

$$_{\mathrm{rot}}\overline{H}_{\mathrm{f}}^{\mathrm{t}}(t) = \frac{|H_x|e^{i\psi_x} + j|H_y|e^{i\psi_y}}{\sqrt{2}}g(t) \quad [\mathrm{A.5}]$$

$$= \frac{H_x^* + jH_y^*}{\sqrt{2}}g(t) \quad [\mathrm{A.6}]$$

$$= \left(H_{\mathrm{f}}^{\mathrm{t}}\right)^* g(t) \quad [\mathrm{A.7}]$$

Hence, using the definitions given in (1), the flip angle is defined in terms of the phasor domain rms magnetic field as Eq. A.8:

$$\alpha(\mathbf{r}, t) = \gamma\mu|H_{\mathrm{f}}^{\mathrm{t}}|\int_{\mathrm{pulse}} g(t)\,\mathrm{d}t \quad [\mathrm{A.8}]$$

APPENDIX B: CYLINDRICAL SAMPLES

In this section, the rotating magnetic field magnitude per square-root of the total absorbed power for a cylindrical sample will be found using cylindrical basis functions. The reasons for the choice of basis functions are two-fold. First, the accuracy increases because the functions are

more suitable to the geometry of interest (as mentioned in the Introduction). Second, it is shown that starting with a full-wave solution and then making a quasi-static assumption leads to the same dependence on sample properties as starting with the quasi-static assumption and using the corresponding basis functions.

Electric Field Expressions inside the Sample

Consider a circularly cylindrically shaped, isotropic and homogeneous sample with the complex propagation constant $k = \sqrt{-j\omega_0\mu(\sigma + j\omega_0\epsilon)}$. $\hat{\mathbf{z}}$-components of the electric and magnetic fields inside this sample can be found by solving the source-free Helmholtz Equation, yielding the following equations (31):

$$E_z(\rho, \phi, z) = \sum_{m=-\infty}^{\infty} \sum_{n=-\infty}^{\infty} A_{mn} J_m(k_\rho \rho) e^{jm\phi} e^{-j\frac{2\pi n}{L}z} \quad [\text{B.1}]$$

$$H_z(\rho, \phi, z) = \sum_{m=-\infty}^{\infty} \sum_{n=-\infty}^{\infty} -j B_{mn} J_m(k_\rho \rho) e^{jm\phi} e^{-j\frac{2\pi n}{L}z} \quad [\text{B.2}]$$

where m and n are the rotational and longitudinal mode numbers, respectively, L is the sample length, $k_\rho = \sqrt{k^2 - (2\pi n/L)^2}$ is the radial propagation constant, and the $J_m(k_\rho \rho)$ terms are cylindrical Bessel functions of the first kind and order m with A_{mn} and B_{mn} being the corresponding field coefficients. $Y_m(k_\rho \rho)$ terms (Bessel functions of the second kind and order m), which are also solutions to the Helmholtz equation, cannot be included because the region of interest in this study includes $\rho = 0$ and $Y_m(0) \to \infty$. Using Eqs. B.1–B.2 and applying Maxwell's equations as given in Ref. (32), the transverse field components can be obtained and put into matrix form:

$$\mathbf{E}(\rho, \phi, z) = \sum_{m=-\infty}^{\infty} \sum_{n=-\infty}^{\infty} [\hat{\rho} \quad \hat{\phi} \quad \hat{\mathbf{z}}]_{1\times3} \mathbf{E}_{mn} \mathbf{a}_{mn} e^{jm\phi} e^{-j\frac{2\pi n}{L}z}$$

$$[\text{B.3}]$$

where

$$\mathbf{E}_{mn}(\rho, \phi, z) = \begin{bmatrix} -\dfrac{j2\pi n}{Lk_\rho} J'_m(k_\rho \rho) & \dfrac{mk^2}{\sigma'\rho k_\rho^2} J_m(k_\rho \rho) \\[2mm] \dfrac{2\pi nm}{L\rho k_\rho^2} J_m(k_\rho \rho) & \dfrac{jk^2}{k_\rho \sigma'} J'_m(k_\rho \rho) \\[2mm] J_m(k_\rho \rho) & 0 \end{bmatrix}_{3\times2}$$

$$[\text{B.4}]$$

$$\mathbf{a}_{mn} = \begin{bmatrix} A_{mn} \\ B_{mn} \end{bmatrix}_{2\times1}$$

and $\sigma' = \sigma + j\omega_0\epsilon$. In B.3, $\mathbf{E}_{mn}$ contains the cylindrical expansion functions for the electric field in $\hat{\rho}, \hat{\phi}, \hat{\mathbf{z}}$ directions for modes (m, n), and $\mathbf{a}_{mn}$ contains the corresponding coefficients.

Implementing the magnetic field components derived using Maxwell's Equations from Eq. B.2 into A.3, the total forward-polarized magnetic field (in reception) can be found:

$$H_f^r(\rho, \phi, z) = \sum_{n=-\infty}^{\infty} \sum_{m=-\infty}^{\infty} \frac{1}{\sqrt{2}k_\rho}$$

$$\times \left(j\sigma' A_{mn} + \frac{2\pi n}{L} B_{mn} \right) J_{m+1}(k_\rho \rho) e^{j(m+1)\phi} e^{-j\frac{2\pi n}{L}z}$$

$$= \sum_{n=-\infty}^{\infty} \sum_{m=-\infty}^{\infty} \mathbf{b}_{mn} \mathbf{a}_{mn} \quad [\text{B.5}]$$

where

$$\mathbf{b}_{mn} = \frac{1}{\sqrt{2}k_\rho} \begin{bmatrix} j\sigma' & \dfrac{2\pi n}{L} \end{bmatrix}_{1\times2} J_{m+1}(k_\rho \rho) e^{j(m+1)\phi} e^{-j\frac{2\pi n}{L}z} \quad [\text{B.6}]$$

are the rotating magnetic field expansion functions. Similarly, the forward-polarized rotating magnetic field in transmission can be obtained:

$$H_f^t(\rho, \phi, z) = \sum_{n=-\infty}^{\infty} \sum_{m=-\infty}^{\infty} \frac{1}{\sqrt{2}k_\rho}$$

$$\times \left(j\sigma' A_{mn} - \frac{2\pi n}{L} B_{mn} \right) J_{m-1}(k_\rho \rho) e^{j(m-1)\phi} e^{-j\frac{2\pi n}{L}z}. \quad [\text{B.7}]$$

Power Definition

Using Eq. B.3 in Eq. 3, the absorbed power in a uniform cylindrical sample becomes the following:

$$P = \int_{-L/2}^{L/2} \int_0^{2\pi} \int_0^{R_0} \sigma \mathbf{E}^H(\rho, \phi, z) \cdot \mathbf{E}(\rho, \phi, z) \rho \, d\rho \, d\phi \, dz \quad [\text{B.8}]$$

where superscript H denotes the Hermitian (i.e., complex conjugate transpose) operator and "·" is the standard dot product (28). In Eq. B.8, there are four summations, namely over m, n, m', and n' such that cross-correlation terms can be calculated. However, due to the exponential functions along z and ϕ in Eq. B.3, the correlation of two electric field modes (m, n) and (m', n') is zero, unless $m = m'$ and $n = n'$, which leads to $k_\rho = k'_\rho$. Thus, the summations over m and n are sufficient. Furthermore, the exponential terms cancel out due to the Hermitian operation. The integrals can be interchanged with the summations over the modes and after making some algebraic manipulations the absorbed power is expressed as the following:

$$P = \sum_{n=-\infty}^{\infty} \sum_{m=-\infty}^{\infty} \int_{-L/2}^{L/2} \int_0^{2\pi} \int_0^{R_0} \left(\mathbf{a}_{mn}^H \mathbf{E}_{mn}^H \mathbf{E}_{mn} \mathbf{a}_{mn} \right) \sigma \rho \, d\rho \, d\phi \, dz$$

$$= \sum_{n=-\infty}^{\infty} \sum_{m=-\infty}^{\infty} \mathbf{a}_{mn}^H \mathbf{R}_{mn} \mathbf{a}_{mn} \quad [\text{B.9}]$$

where $\mathbf{R}_{mn}$ is a 2×2 matrix and is given by the expression:

$$\mathbf{R}_{mn} = \int_{-L/2}^{L/2} \int_0^{2\pi} \int_0^{R_0} \mathbf{E}_{mn}^H \mathbf{E}_{mn} \sigma \rho \, d\rho \, d\phi \, dz.$$

$$= 2\pi\sigma L \int_0^{R_0} \mathbf{E}_{mn}^H \mathbf{E}_{mn} \rho \, d\rho. \quad [\text{B.10}]$$

To maximize SNR and/or minimize SAR, $\xi = H_f^r/\sqrt{P}$ should be maximized. Thus, either the absorbed power should be minimized, or the signal (i.e., the rotating magnetic field H_f^r) should be maximized. In this study, the magnetic field at the POI is fixed, and the minimum possible power is found with the Lagrange Multipliers Method (33) using the same approach that was previously employed in Refs. (7,12). The resulting expression for the minimum absorbed power is Eq. B.11:

$$P_{\min} = \left[\sum_{n=-\infty}^{\infty} \sum_{m=-\infty}^{\infty} \mathbf{b}_{mn} \mathbf{R}_{mn}^{-1} \mathbf{b}_{mn}^H \right]^{-1} \left| H_f^r \right|^2. \qquad [B.11]$$

Implementing $\mathbf{E}_{mn}(\rho, \phi, z)$ from Eq. B.4 into B.10 and using the resulting expression with b_{mn} from B.6 in B.11, the minimum absorbed power can be expressed as Eq. B.12:

$$P_{\min} = \left[\sum_{n=-\infty}^{\infty} \sum_{m=-\infty}^{\infty} \frac{|J_{m+1}(k_\rho \rho)|^2}{4\pi \, \sigma L |k_\rho|^2} \frac{G_{\text{num}}(m,n)}{G_{\text{den}}(m,n)} \right]^{-1} \left| H_f^r \right|^2$$

[B.12]

where

$$G_{\text{num}}(m,n)$$

$$= \frac{1}{2} Q(m-1,n) \left[|k|^4 + \left(\frac{2\pi n}{L}\right)^4 + 2\left(\frac{2\pi n}{L}\right)^2 \Re\{k^2\} \right]$$

$$+ \frac{1}{2} Q(m+1,n) \left[|k|^4 + \left(\frac{2\pi n}{L}\right)^4 - 2\left(\frac{2\pi n}{L}\right)^2 \Re\{k^2\} \right]$$

$$+ Q(m,n) \left| \frac{2\pi n k_\rho}{L} \right|^2 \qquad [B.13]$$

$$G_{\text{den}}(m,n) = \frac{1}{2}(\omega_0 \mu)^2 [Q(m,n)Q(m-1,n)$$

$$+ Q(m,n)Q(m+1,n) + 2Q(m-1,n)Q(m+1,n)] \quad [B.14]$$

and

$$Q(m,n) = \int_0^{R_0} |J_m(k_\rho \rho)|^2 \rho \, d\rho, \qquad [B.15]$$

with $\Re\{k^2\}$ being the real part of k^2. Using the following identity [given in (39)]:

$$\int_0^{R_0} J_m(k_\rho \rho) J_m^*(k_\rho \rho) \rho \, d\rho$$

$$= \frac{\rho}{k_\rho^2 - k_\rho^{*2}} \left\{ k_\rho J_m\!\left(k_\rho^* \rho\right) J_{m+1}(k_\rho \rho) - k_\rho^* J_m(k_\rho \rho) J_{m+1}\!\left(k_\rho^* \rho\right) \right\} \Big|_0^{R_0}$$

[B.16]

$Q(m,n)$ is found in closed-form as the following:

$$Q(m,n) = \frac{R_0}{4j\Re\{k_\rho\}\Im\{k_\rho\}}$$

$$\times \left\{ k_\rho J_m\!\left(k_\rho^* R_0\right) J_{m+1}(k_\rho R_0) - k_\rho^* J_m(k_\rho R_0) J_{m+1}\!\left(k_\rho^* R_0\right) \right\}$$

where $\Im\{k_\rho\}$ is the imaginary part of k_ρ. Performing a series expansion for each Bessel function and making

some algebraic manipulations, $Q(m,n)$ can be expressed as Eq. B.17

$$Q(m,n) = R_0^2 \frac{1}{2} \sum_{a=0}^{\infty} \sum_{b=0}^{\infty} \left| \frac{k_\rho R_0}{2} \right|^{4b+2a+2|m|}$$

$$\times \frac{(a+1)^2}{(b)!(b+|m|)!(b+a+1)!(b+a+1+|m|)!}. \quad [B.17]$$

It should be kept in mind that k_ρ is a function of n in B.17. If the object is smaller than the wavelength ($L \ll \lambda$), the conductivity is not very high [a valid assumption for samples that are imaged using MRI (34,35)] and $n \neq 0$, then the longitudinal propagation constant $2\pi n/L$ becomes very large in magnitude compared to the wavenumber k. Hence, the approximation $k_\rho \simeq -j2\pi n/L$ can be made. To guarantee that the electromagnetic field decays as it propagates in the transverse plane away from the axis of the sample, the negative branch of the square root is chosen. On the other hand, when $n = 0$, the field propagates only radially, yielding $k_\rho = k$. In this case (i.e., $n = 0$), due to the assumptions that $R_0 \ll L \ll \lambda$ and $\left| k_\rho R_0 \right| \ll 1$, retaining only the first terms of the summations ($a = b = 0$) in B.17 yields converged results. Expressing L/R_0 as ζ, $Q(m,n)$ is obtained:

$$Q(m,n) = \begin{cases} R_0^2 f(m,n) & \text{if } n \neq 0 \\[2mm] R_0^{2+2|m|} \frac{1}{2} \left| \frac{k}{2} \right|^{2|m|} \frac{1}{(|m|)!(1+|m|)!} & \text{if } n = 0 \end{cases}$$

[B.18]

where

$$f(m,n) = \frac{1}{2} \sum_{a=0}^{\infty} \sum_{b=0}^{\infty} \left(\frac{\pi n}{\zeta}\right)^{4b+2a+2|m|}$$

$$\times \frac{(a+1)^2}{(b)!(b+|m|)!(b+a+1)!(b+a+1+|m|)!}. \quad [B.19]$$

In most applications, the region of interest in MRI imaging includes the axis of the object to be imaged. Furthermore, it was previously shown that for external coils, UISNR is lowest on the axis (12). To find the lowest upper bound on the ISNR, the POI is selected to be on the axis of the sample. On the axis of the object to be imaged, all rotational modes of H_f^r (given by Eqs. B.5–B.6 in Appendix B), except $m = -1$, contribute to the noise (Power Definition section in Appendix B, Eqs. B.9–B.10) but not to the signal. Thus, when the optimum field coefficients for the maximum SNR on the axis are calculated, only the $m = -1$ mode has a nonzero coefficient. Using this fact, the infinite summation over m can be avoided by retaining only $m = -1$. As a result, the minimum absorbed power on the axis ($\rho = 0$) can be expressed:

$$P_{\min,\text{axis}} = \sigma(\omega_0 \mu)^2 R_0^5 \frac{1}{\sum_{n=-\infty}^{\infty} h(-1,n)} \left| H_f^r \right|^2 \qquad [B.20]$$

where

$$h(-1, n) = \frac{1}{\pi\zeta} \begin{cases} \left(\frac{\pi n}{\zeta}\right)^2 \frac{(f(0, n) + f(-2, n) + 2f(-1, n))}{(f(-1, n)f(0, n) + f(-1, n)f(-2, n) + 2f(0, n)f(-2, n))}, & \text{if } n \neq 0 \\ 2^2, & \text{if } n = 0. \end{cases}$$ [B.21]

For a lossy medium (i.e., $\sigma \neq 0$), the electromagnetic field decays as it propagates. For the range of conductivity values that are encountered in MRI (34,35), the length at which the electromagnetic field decays to negligible levels is found to be $L > 4R_0$. Hence, if this condition is met, the sample's length does not affect the absorbed power and, hence, the SNR. Furthermore, due to the factorial functions in the denominator of Eq. B.19 and the order of the denominator of Eq. B.21 being higher than the numerator, the infinite summation over the longitudinal mode number n that appears in the denominator of B.20 converges rapidly to a constant with a finite number of longitudinal modes. The authors observed that the necessary number of modes is ~ 25 when the POI is on the axis, which can increase to above 200 when the POI approaches the surface. Furthermore, when the POI moves away from the origin, the required number of circumferential modes increases to approximately 250 when the surface is approached. When the POI is very close to the surface, numerical error is introduced into the calculations because the expansion is for cylindrical structures, and the effective medium seen is a semi-infinite plane (which is addressed in Section Practical Implementation: Cylindrical Samples). Even if the condition $L > 4R_0$ fails, the error it introduces remains below 5%. Replacing the summation in Eq. B.20 by the obtained constant value, the minimum absorbed power expression given by B.20 can be expressed:

$$P_{\text{min,axis}} = 0.9332\sigma(\omega_0\mu)^2 R_0^5 |H_f^r|^2.$$ [B.22]

Then, the rotating magnetic field magnitude per square-root of total absorbed power at the POI, which was defined in Eq. 6, can be expressed:

$$\xi = \frac{1}{\sqrt{0.9332\sigma(\omega_0\mu)^2 R_0^5}} = \mathcal{S}_{\text{max}} \frac{1}{\omega_0\mu\sqrt{\sigma}} R_0^{-2.5}$$ [B.23]

where the shape factor is $\mathcal{S}_{\text{max}} = 1.035$, and the size factor is the radius of the cylinder.

REFERENCES

1. Prince JL, Links JM. Medical imaging signals and systems. Pearson Prentice Hall: New Jersey; 2006.
2. Mueller OM, General Electric. Unconditionally stable ultra low noise RF preamplifier. US Patent 4,835,485 (1989).
3. Edelstein WA, Glover GH, Hardy CJ, Redington RW. The intrinsic signal-to-noise ratio in NMR imaging. Magn Reson Med 1986;3:604–618.
4. Seton HC, Hutchison JMS, Bussell DM. A 4.2 K receiver coil and SQUID amplifier used to improve the SNR of low-field magnetic resonance images of the human arm. Meas Sci Tech 1997;8:198–207.
5. Wright AC, Song HK, Wehrli FW. In vivo MR micro imaging with conventional radiofrequency coils cooled to 77K. Magn Reson Med 2000;43:163–169.
6. Black RD, Early TA, Roemer RP, Mueller OM, Mogro-Campero A, Turner LG, Johnson GA. A high-temperature superconducting receiver for nuclear magnetic resonance microscopy. Science 1993;259:793–795.
7. Ocali O, Atalar E. Ultimate intrinsic signal to noise ratio in MRI. Magn Reson Med 1998;39:462–473.
8. Lattanzi R, Sodickson DK, Grant AK, Zhu Y. Electrodynamic constraints on homogeneity and radiofrequency power deposition in multiple coil excitations. Magn Reson Med 2009;61:315–334.
9. Hoult DI, Richards RE. The signal-to-noise ratio of the nuclear magnetic resonance experiment. J Magn Reson 1976;24:71–85.
10. Hoult DI. The principle of reciprocity in signal strength calculations—a mathematical guide. Concepts Magn Reson 2000;12:173–187.
11. Lattanzi R, Grant AK, Ohliger MA, Sodickson DK. Measuring practical coil array performance with respect to ultimate intrinsic SNR: a tool for array design and assessment. Proceedings of the 14th Annual Meeting of ISMRM, Seattle, Washington, USA, 2006. p. 424.
12. Celik H, Eryaman Y, Altintas A, Abdel-Hafez IA, Atalar E. Evaluation of internal MRI coils using ultimate intrinsic SNR. Magn Reson Med 2004;52:640–649.
13. Vesselle H, Collin RE. The signal-to-noise ratio of nuclear magnetic resonance surface coils and application to a lossy dielectric cylinder model–part I: theory. IEEE Trans Biomed Eng 1995;42:497–506.
14. Ohliger MA, Grant AK, Sodickson DK. Ultimate intrinsic signal-to-noise ratio for parallel MRI: electromagnetic field considerations. Magn Reson Med 2003;50:1018—1030.
15. Wiesinger F, De Zanche N, Pruessmann KP. Approaching ultimate SNR with finite coil arrays. Proceedings of the 13th Annual Meeting of ISMRM, Miami Beach, Florida, USA, 2005. p. 672.
16. Wiesinger F, Boesiger P, Pruessmann KP. Electrodynamics and ultimate SNR in parallel MR imaging. Magn Reson Med 2004;52:376—390.
17. Schnell W, Renz W, Vester M, Ermert H. Ultimate signal-to-noise-ratio of surface and body antennas for magnetic resonance imaging. IEEE Trans Antennas Proping 2000;48:418–428.
18. Lattanzi R, Grant AK, Sodickson DK. Approaching ultimate SNR and ideal current patterns with finite surface coil arrays on a dielectric cylinder. Proceedings of the 16th Annual Meeting of ISMRM, Toronto, Ontario, Canada, 2008. p. 1074.
19. Lattanzi R, Sodickson DK. Dyadic Green's functions for electrodynamic calculations of ideal current patterns for optimal SNR and SAR. Proceedings of the 16th Annual Meeting of ISMRM, Toronto, Ontario, Canada, 2008. p. 78.
20. Lattanzi R, Grant AK, Polimeni JR, Ohliger MA, Wiggins GC, Wald LL, Sodickson DK. Performance evaluation of a 32-element head array with respect to the ultimate intrinsic SNR. NMR Biomed 2010;23: 142–151.
21. Eryaman Y, Tunc CA, Atalar E, Minimum SAR for RF shimming by allowing spatial phase variation. Proceedings of the 17th Annual Meeting of ISMRM, Honolulu, Hawaii, USA, 2009, p. 4777.
22. Hoult DI, Lauterbur PC. The sensitivity of the zeugmatographic experiment involving human samples. J Magn Reson 1979;343:425–433.
23. Wang J, Reykowski A, Dickas J. Calculation of the signal-to-noise ratio for simple surface coils and arrays of coils. IEEE Trans Biomed Eng 1995;42:908–917.
24. Reykowski A, Wright SM. The SNR of the idealized birdcage resonators and the SNR limit for infinite cylinder arrays. Proceedings of the 3rd Annual Meeting of ISMRM, Nice, France, 1995. p. 974.
25. Reykowski A. Theory and design of synthesis array coils for magnetic resonance imaging. Dissertation, Texas A&M University, December 1996.
26. Kopanoglu E, Erturk VB, Atalar E, A closed-form expression for ultimate intrinsic signal-to-noise ratio in MRI, Proceedings of the 17th Annual Meeting of ISMRM, Honolulu, Hawai'i, USA, 2009, p. 2975.
27. Balanis CA. Antenna theory analysis and design, 3rd ed. Wiley: New Jersey, 2005.

28. Cheng DK. Fundamentals of engineering electromagnetics. Pearson Addison Wesley: Massachusetts, 1993.

29. IEC, International Standard, Medical equipment – part 2: particular requirements for the safety of magnetic resonance equipment for medical diagnosis, 2nd revision, 601-2-33. International Electrotechnical Commission, Geneva, 2002.

30. FDA, Guidance for the Submission Of Premarket Notifications for Magnetic Resonance Diagnostic Devices, November 14, 1998.

31. Schelkunoff SA. Electromagnetic waves. Bell Telephone Labs Series, New York, 1943.

32. Pozar DM. Microwave engineering. 3rd Ed. Wiley: Massachusetts, 2005.

33. Thomas GB Jr, Finney RL. Calculus and analytic geometry. Addison Wesley: Massachusetts, 1998.

34. Geddes LA, Baker LE. The specific resistance of biological material—a compendum of data for the biomedical engineer and physiologist. Med Biol Eng 1967,5:271–293.

35. Gabriel S, Lau RW, Gabriel C. The dielectric properties of biological tissues: II. Measurements in the frequency range 10 Hz to 20 GHz. Phys Med Biol 1996;41:2251–2269.

36. Macovski A. Noise in MRI. Magn Reson Med 1996;36:494–497.

37. Celik H, Uluturk A, Tali T, Atalar E. A catheter tracking method using reversed polarization for MR-guided interventions. Magn Reson Med 2007;58:1224–1231.

38. Wright SM, Wald LL. Theory and application of array coils in MR spectroscopy. NMR Biomed 1997;10:394–410.

39. McLachlan NW. Bessel functions for engineers. Oxford Engineering Science Series; The Clarendon Press, Oxford, 1955.